INTERNATIONAL JOURNAL FOR NUMERICAL METHODS IN FLUIDS
Int. J. Numer. Meth. Fluids 2002; **39**:607–637 (DOI: 10.1002/fld.345)

Velocity field after wave breaking

Yasunori Watanabe*,† and Hiroshi Saeki

Hydraulic Engineering Laboratory, Hokkaido University, Sapporo, Japan

SUMMARY

The velocity field in breaking water waves is considered in this paper. A numerical simulation describes in detail the transition from a primary overturning and consequent rebounding jets into a bore front, where the vorticity in the coherent large-scale eddy structures devolves into turbulence. Spatial changes in the frequency spectra of the kinetic energy and the enstrophy are associated with the production, transport and dissipation of the Reynolds stress and the various wave and turbulent mixing length scales. Mean velocity fields and the wave and kinetic energy in a surf zone are evaluated. Fourier and wavelet spectral analysis is applied to study both the surface elevation and energy changes, and the distinction that must be made between spilling and plunging breakers is clarified in this paper. Copyright © 2002 John Wiley & Sons, Ltd.

KEY WORDS: wave breaking; large-scale eddy; plunging jet; surf zone

1. INTRODUCTION

Breaking water waves may cause various coastal problems, including sand drift, beach erosion, and damage to coastal structures. During the splash-up cycle of the stronger breaking waves in particular, anisotropic turbulence is produced by overturning plunging jets, in a process where initial large-scale eddies (due to impact transport of momentum) at several plunging points are advected by the wave front and decompose into smaller eddies. This turbulence occurs in addition to that associated with other eddies, continuously produced at the wave front by shear as the wave propagates.

Several breaker types have been classified by others—referred to as spilling, plunging, collapsing and surging, respectively [1]. In a spilling breaker, the broken wave propagates with weak turbulence near the wave crest in a transition region (the outer region) and fully developed turbulence in a bore front (the inner region). Overturning jets in a spilling breaker are relatively small, so turbulence is produced relatively slowly, such that its production and dissipation is almost in balance in the transition region. Wave breaking occurs only above the wave trough level, and the direct contribution by eddies to the fluid motion beneath this level is small. In a plunging breaker however, overturning jets plunge into the water ahead

* Correspondence to: Y. Watanbe, Hydraulic Engineering Laboratory, School of Engineering, Hokkaido University, N-13 W-8, Sapporo 060-8628, Japan.
† E-mail: yasunori@eng.hokudai.ac.jp

Received November 2000
Revised November 2001

of the wave, and on rebounding on the water surface the jets repeatedly splash up until their kinetic energy is sufficiently dissipated. Following this splash-up cycle, a strongly turbulent bore front forms, which is similar to the front in the bore region of a spilling breaker.

The large-scale eddies produced by each plunging jet during the splash-up cycle affect the velocity field in the total surf zone, and are commonly associated with undertow and nearshore currents or sediment suspension. Given the potential for beach erosion, it is important to clarify the generation, transport and dissipation of wave turbulence—especially in the case of the potentially more damaging plunging breaker. Little is known experimentally about the fluid motion after wave breaking however, including the interactions among the eddies of various sizes, because whatever the breaker type it is difficult to measure the fluid velocity field due to the many air bubbles that become entrained. On the other hand, mathematical modelling and numerical simulation may be used to predict the wave fields, and hence derive useful information about beach erosion processes.

There have been many theoretical papers on wave decay after wave breaking, and various associated breaking wave models (e.g. References [2, 3]). The most engineering approach has been based on the bore model [4, 5], where the energy dissipation rate is associated with the broken wave height and an experimental coefficient, assuming significant eddies are not produced. Battjes and Janssen [6] extended this bore model to express the wave decay in the irregular wave field. Such models evidently can only apply to the spilling breaker, and even in that case the velocity field cannot be estimated correctly since generated eddies make a significant contribution to the fluid motion. This approach is clearly inappropriate to describe a plunging breaker, where the large-scale eddies decompose but other smaller scale eddies remain. Thus it is desirable to develop another wave breaking model, preferably independent of breaker type, to predict the fluid velocity throughout the surf zone.

Svendsen and Madsen [7] investigated the bore profile and its development in the bore region, by assuming a simple velocity profile in and underneath the turbulent bore, based on the isotropic eddy viscosity model. Okayasu *et al.* [8] consequently presented an eddy viscosity model, which introduces turbulence in estimating the mean velocity field. It is difficult to validate coefficients concerned with the length scale of turbulence in the bore however, because it is difficult to measure fluid velocity near the surface and uncertainty due to the air bubble entrainment. Furthermore, since the large-scale eddies exhibit unsteady anisotropic turbulence with a high shear, it is questionable whether turbulence in the surf zone diffuses isotropically. It has also been pointed out that a linear eddy viscosity model does not adequately describe anisotropic turbulence, since excess turbulent diffusion is predicted [9].

Since any such wave breaking model involves somewhat simplistic representations for the turbulence, there has been further research. Recently, Ting and Kirby [10] experimentally investigated both the temporal and spatial characteristics of each term in the turbulent kinetic energy equation and the fluctuation scale of the kinetic energy, using a Laser Doppler velocimeter (LDV) and spectral analysis. This indicated that a better treatment of turbulent transport and diffusion is essential to resolve the length scale of eddies in a spilling breaker, with the kinetic energy spectra suggesting a $-3/5$ slope for frequencies in the inertial range.

Although LDV measurements give useful information, especially beneath the wave trough level [11, 12], it remains uncertain whether the actual fluid motion in a plunging jet and a bore front (the source of turbulence) can be found experimentally, due to air bubbles. The velocity at many points in space and time is required to determine the length scale of eddies, where there are large velocity gradients. Moreover, the eddy production and eddy interactions which

occur in any breaking wave evidently vary considerably, and ideally the velocity field should be known continuously in space and time to understand eddy development and turbulence.

Several numerical studies have therefore been attempted. Sakai *et al*. [13] simulated a broken wave by the SMAC method. Park and Miyata [14] treat free surface flow as a liquid–gas two-phase flow using the marker density method, and they estimated the deformation of waves after wave breaking. These authors distinguish the free surface with markers however, which not only leave the free surface or interface somewhat obscure but also induce numerical diffusion when there is a complex free surface profile such as in a overturning jet, since the precision depends upon the number of markers in each cell. Thus their calculations apply to relatively small-scale wave breaking with a small overturning jet, and to date there does not appear to be any successful simulation of large scale wave breaking—e.g. for a high breaking wave or a steep bottom slope.

Lin and Liu [15, 16] used the non-linear k–ε model to simulate the production, transport and dissipation processes of turbulence and Reynolds stress in the surf zone. They investigated the time and space dependence of each term in the model, and pointed out that these processes are quite different at cross sectional level, which depends on the development of the breaking wave. Furthermore, they discussed the properties of turbulence in the plunging breaker, and the dependence on the breaker type. In this and earlier papers, they focus on the characteristics of the fluid velocity and turbulent energy but less on either the large-scale or smaller induced eddies through the splash-up cycle, which are important in the production and transport of turbulence in the transition region.

The eddy structure and its scale depend not only on breaker type but also on each region in the surf zone. The coherent structure produced in the transition region develops into the complex structure distributed over a wide area in the bore region, through interactions between the eddies and the turbulent diffusion. A proper evaluation of turbulence is essential to estimate the velocity field in the surf zone.

In this paper, the simulation is based upon the fundamental Navier–Stokes equation. In order to satisfactorily represent the impulsive fluid motion near the onset of a plunging jet, the non-linear terms in the Navier–Stokes equation must be evaluated quite accurately, because truncation errors in these terms may introduce numerical diffusion and implicit artificial viscosity (see for example Reference [17]). The cubic-polynomial interpolation (CIP) method, proposed by Yabe *et al*. [18–20] to solve hyperbolic differential equations is adopted, to produce the two-dimensional velocity field in the surf zone and hence the fundamental properties of turbulence, large-scale eddies and Reynolds stress in modelling wave breaking from the depth-averaged wave equation reported here. The numerical methods and the boundary conditions applied are explained in Section 2. In Section 3.1, the numerical results obtained are compared with solutions from cnoidal wave theory and experimental measurements. Section 3.2 is devoted to discussion of the instantaneous fluid motion during the large-scale wave breaking, the production and transportation of large-scale eddies through the splash-up cycle, and the interactions between the eddies of various sizes. The frequency spectra of the kinetic energy and the enstrophy, and the progression from large-scale eddies to the smaller scale turbulence, is discussed in Section 3.3. The discussion in Section 3.4 concerns the production, transport and dissipation processes of the Reynolds stress, and whether any eddy viscosity model may be applicable in this context. With reference to the undertow which breaking waves produce, the mean velocity field is investigated in Section 3.5. Finally, in Section 3.6 there is discussion of the spatial wave number properties of the surface elevation,

mean kinetic energy and turbulent energy integrated over depth throughout the surf zone—to determine the length and velocity scale in the cross-shore direction, based on wavelet analysis. All these investigations were conducted with both plunging and spilling breakers in mind, with respective results described in each case. In passing we note that Nadaoka *et al.* [21] report that a three-dimensional eddy structure (with obliquely descent eddies) produces substantial sediment suspension, so extension of the numerical simulation to three dimensions is warranted—but the two-dimensional simulation gives important information on potentially damaging horizontal roller eddies, which are predominantly associated with breaking waves featuring overturning jets.

2. NUMERICAL METHOD

2.1. Computational procedures

A beach of uniform slope is considered, with constant inclination angle θ as shown in Figure 1. The governing Navier–Stokes equation is

$$\frac{D\mathbf{u}}{Dt} = -\nabla p + \frac{1}{\mathrm{Re}}\nabla^2\mathbf{u} + \mathbf{g} \tag{1}$$

where $\mathbf{u}$ denotes fluid velocity, p the pressure, $\mathbf{g}$ constant gravitational acceleration, and Re the Reynolds number. In terms of the coordinate system (s,n) in Figure 1, we have

$$\frac{D}{Dt} = \frac{\partial}{\partial t} + u^*\frac{\partial}{\partial s} + v^*\frac{\partial}{\partial n}, \quad \nabla = \left(\frac{\partial s}{\partial x}\frac{\partial}{\partial s} + \frac{\partial n}{\partial y}\frac{\partial}{\partial n}, \frac{\partial n}{\partial x}\frac{\partial}{\partial n} + \frac{\partial s}{\partial y}\frac{\partial}{\partial s}\right), \quad \nabla^2 = \frac{\partial^2}{\partial s^2} + \frac{\partial^2}{\partial n^2},$$

$$u^* = u\frac{\partial s}{\partial x} + v\frac{\partial s}{\partial y}, \quad v^* = u\frac{\partial n}{\partial x} + v\frac{\partial n}{\partial y}, \quad \frac{\partial s}{\partial y} = -\frac{\partial n}{\partial x} = \sin\theta, \quad \frac{\partial s}{\partial x} = \frac{\partial n}{\partial y} = \cos\theta$$

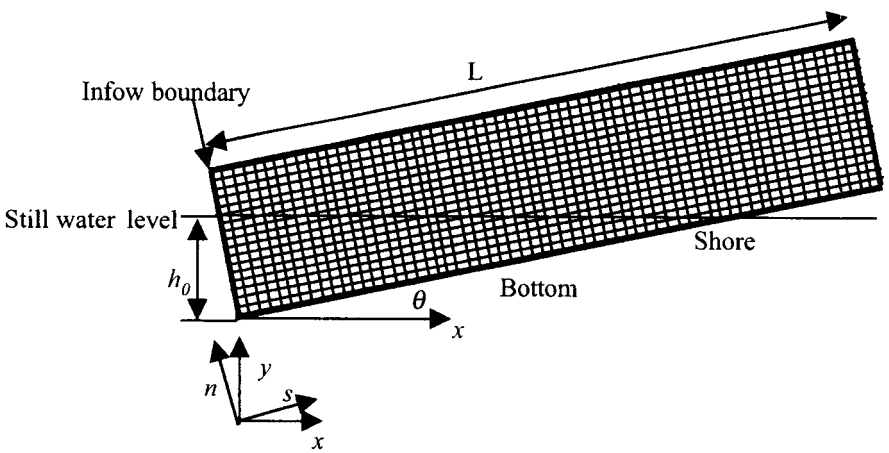

Figure 1. Computational domain and co-ordinate system.

where the asterisk denotes quantities relative to the (s,n) co-ordinates. All variables in (1) have been normalized by wave celerity (C), water depth at the inflow boundary (h_0) and water density (ρ_w).

The numerical solution procedure adopted in this paper involves time splitting on the basis of a fractional two-step technique [18], where (1) is solved in two phases—namely,

the non-advection phase

$$\frac{\partial \mathbf{u}}{\partial t} = -\frac{1}{\rho}\nabla p + \frac{1}{\mathrm{Re}}\nabla^2 \mathbf{u} + \mathbf{g} \tag{2}$$

and the advection phase

$$\frac{D\mathbf{u}}{Dt} = 0 \tag{3}$$

Thus the discrete form of (1) at the intermediate time step $n+1/2$

$$\frac{\mathbf{u}^{n+1} - \mathbf{u}^n}{\Delta t} + [(\nabla \mathbf{u})\mathbf{u}]^{n+1/2} = (\mathrm{RHS})^{n+1/2} \tag{4}$$

is equivalent to the sum of the equations

$$\frac{\mathbf{u}^{n+1/2} - \mathbf{u}^n}{\Delta t} = (\mathrm{RHS})^{n+1/2} \tag{5}$$

$$\frac{\mathbf{u}^{n+1} - \mathbf{u}^{n+1/2}}{\Delta t} + [(\nabla \mathbf{u})\mathbf{u}]^{n+1/2} = 0 \tag{6}$$

It is immediately seen that (5) and (6) express the discrete forms of (2) and (3), respectively.

In the non-advection phase, the discrete form of (2) is divided into the discrete forms of the following two equations, based on the fractional two-step method:

$$\frac{\mathbf{u}' - \mathbf{u}}{\Delta t} = -\frac{1}{\rho}\nabla p' + \mathbf{g} \tag{7}$$

$$\frac{\mathbf{u}'' - \mathbf{u}'}{\Delta t} = \frac{1}{\mathrm{Re}}\nabla^2 \mathbf{u}' \tag{8}$$

On taking the divergence of (7) and setting $\nabla \cdot \mathbf{u}'' = 0$ to ensure the velocity at the next time step is not divergent, we solve a Poisson equation for the pressure

$$\nabla^2 p' = -\rho \frac{\partial d}{\partial t} \tag{9}$$

where the divergence of the velocity is

$$d = \frac{\partial s}{\partial x}\frac{\partial u}{\partial s} + \frac{\partial n}{\partial x}\frac{\partial u}{\partial n} + \frac{\partial s}{\partial y}\frac{\partial v}{\partial s} + \frac{\partial n}{\partial y}\frac{\partial v}{\partial n}$$

Many iterative solvers for the Poisson equation (9) have been developed to reduce computational costs (e.g. Incomplete Modified Cholesky Conjugate Gradient Method [22]) and to

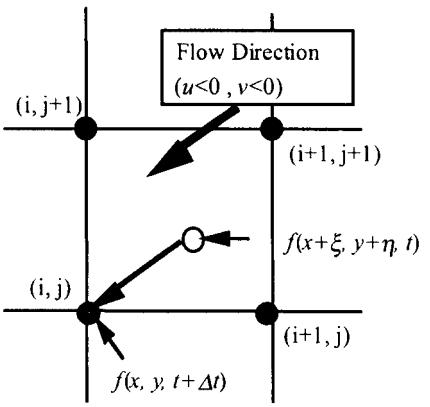

Figure 2. Evaluation of the advection phase equation.

improve performance of the computations (e.g. Multi-grid Method [23, 24]). However, in this paper, a classical successive over-relaxation (SOR) method was employed in computing (9) because an improvement in the iterative computation for a linear equation system is out of the scope of this paper. The velocity given by (7) then updated by the predictor and corrector method [25].

Accurate solution for the strongly non-linear fluid motion at high Reynolds number (accurate evaluation of the non-linear terms) depends upon the extent of implicit artificial viscosity due to numerical truncation error and numerical instability. The advection phase equation (3) was solved by the CIP method proposed by Yabe *et al.* [18] as a numerical solver for the hyperbolic equation, using the velocity field obtained from the non-advection phase equation (2).

Let us therefore outline this CIP method, to numerically solve the differential equation

$$\frac{Df}{Dt} = 0 \tag{10}$$

As shown in Figure 2, the function f and its space derivatives at an arbitrary point $(x+\xi, y+\eta)$ in a rectangular cell with vertices (x, y), $(x+\Delta x, y)$, $(x, y+\Delta y)$ and $(x+\Delta x, y+\Delta y)$ are interpolated by a cubic-polynomial

$$f(x+\xi, y+\eta) = a_1\xi^3 + a_2\xi^2\eta + a_3\xi^2 + a_4\xi\eta + \frac{\partial f(x,y)}{\partial x}\xi + a_5\eta^3 + a_6\eta^2\xi + a_7\eta^2 + \frac{\partial f(x,y)}{\partial y}\eta + f(x,y) \tag{11}$$

$$\frac{\partial f(x+\xi, y+\eta)}{\partial x} = 3a_1\xi^2 + 2a_2\xi\eta + 2a_3\xi + a_4\eta + a_6\eta^2 + \frac{\partial f(x,y)}{\partial x} \tag{12}$$

$$\frac{\partial f(x+\xi, y+\eta)}{\partial y} = 3a_5\eta^2 + 2a_6\xi\eta + 2a_7\eta + a_4\xi + a_2\xi^2 + \frac{\partial f(x,y)}{\partial y} \tag{13}$$

where ξ and η are the local co-ordinates that the origin is set at the grid (x, y). Assuming f is a continuous function between vertices, the coefficients a_1–a_7 can be determined as follows:

$$a_1 = \left(2(f(x,y) - f(x+\Delta x, y)) + \left(\frac{\partial f(x,y)}{\partial x} + \frac{\partial f(x+\Delta x, y)}{\partial x}\right)\Delta x\right) \Big/ \Delta x^3$$

$$a_2 = (f(x,y) - f(x, y+\Delta y) - f(x+\Delta x, y) + f(x+\Delta x, y+\Delta y) + \left(\frac{\partial f(x,y)}{\partial x} - \frac{\partial f(x, y+\Delta y)}{\partial x}\right)\Delta x\right) \Big/ \Delta x^2 \Delta y$$

$$a_3 = \left(3(f(x+\Delta x, y) - f(x,y)) - \left(2\,\frac{\partial f(x,y)}{\partial x} + \frac{\partial f(x+\Delta x, y)}{\partial y}\right)\Delta x\right) \Big/ \Delta x^2$$

$$a_4 = (-f(x,y) + f(x, y+\Delta y) + f(x+\Delta x, y) - f(x+\Delta x, y+\Delta y) + \left(-\frac{\partial f(x,y)}{\partial x} + \frac{\partial f(x, y+\Delta y)}{\partial x}\right)\Delta x + \left(-\frac{\partial f(x,y)}{\partial y} + \frac{\partial f(x+\Delta x, y)}{\partial y}\right)\Delta y$$

$$a_5 = \left(2(f(x,y) - f(x, y+\Delta y)) + \left(\frac{\partial f(x,y)}{\partial y} + \frac{\partial f(x, y+\Delta y)}{\partial y}\right)\Delta y\right) \Big/ \Delta y^3$$

$$a_6 = (f(x,y) - f(x, y+\Delta y) - f(x+\Delta x, y) + f(x+\Delta x, y+\Delta y) + \left(\frac{\partial f(x,y)}{\partial x} - \frac{\partial f(x+\Delta x, y)}{\partial y}\right)\Delta y\right) \Big/ \Delta x \Delta y^2$$

$$a_7 = \left(3(f(x, y+\Delta y) - f(x,y)) - \left(2\,\frac{\partial f(x,y)}{\partial y} + \frac{\partial f(x, y+\Delta y)}{\partial y}\right)\Delta y\right) \Big/ \Delta y^2$$

Thus Equation (10) means that $f(x+\xi, y+\eta)$ is advected to the co-ordinate (x, y) by the velocities $u\ (= -\xi/\Delta t)$ and $v\ (= -\eta/\Delta t)$ during a small time interval Δt (see Figure 2), so provided Δt is sufficiently small and the flow field is locally steady, at the next time step f can be updated by setting $f(x, y, t+\Delta t) = f'(x+\xi, y+\eta, t)$. The constants a_1–a_7 depend upon the velocity obtained from the non-advection phase calculation, and the fluid velocity $u = f(x, y, t)$ given by (3) is evaluated from (11) to (13), after ξ and η are obtained from the velocity field in the non-advection phase by setting $\xi = -u\Delta t$, $\eta = -v\Delta t$. Since the interpolation by the spatial derivative of f is worked as a restriction condition on the gradient of f, the sharp profile of f is retained through the advection phase.

A free surface can also be updated by the same procedure, as described in the next section.

2.2. *Boundary conditions*

There have been many surface tracking methods proposed until now (see the detailed review by Scardoveli and Zaleski [26]; Thome *et al.* [27], for example). Volume of fluid (VOF) techniques [28] are widely applied to engineering numerical research (e.g. [16]). The density function method used for tracking a free surface in this paper is similar to the VOF method in terms of the same colour function introduced, while the colour (density) function is directly

Table I. Numerical and wave conditions.

	Breaker type	H/h_0	L/h_0	θ	Re (Ch_0/ν)	Time step interval Δt	Grid spacing ($\Delta x = \Delta y$)
Test	No breaking	0.41	11.5	0.0	575000	$2\pi/512$	0.04
Case 1	Plunging breaker	0.41	11.5	$\mathrm{Tan}^{-1}(1/30)$		$2\pi/2048$	0.03
Case 2	Spilling breaker	0.41	6.0	$\mathrm{Tan}^{-1}(1/30)$		$2\pi/512$	0.03
Case 3	Plunging breaker	0.41	11.5	$\mathrm{Tan}^{-1}(1/15)$		$2\pi/4096$	0.01

updated via Lagrangean advection, which is unlike the VOF technique based on the donor–acceptor method. We use the density function ρ_f which takes the value 1 in a computational cell filled with fluid, 0 in a cell without fluid, and a value between 0 and 1 (namely 0.5) in a cell enclosing a portion of the free surface—i.e. ρ_f is a step function at cells associated with a free surface. For all cells, this density function ρ_f is updated by

$$\frac{D\rho_f}{Dt} = 0 \tag{14}$$

which at a free surface may be regarded as the kinematic boundary condition. Equation (14) is solved by the CIP method, taking $f(x, y, t) = \rho_f$ in (10). A potential drawback is that the free surface may become obscured by numerical diffusion, due to the abrupt change in the density function from 1 to 0 in cells at a free surface, and acceptable accuracy in the calculation of the spatial derivatives requires a sufficiently fine grid. However, we found that a free surface can be well defined even if it has a complex shape such as an overturning jet, because although the density function is a step function it is well represented with the derivatives in each cell interpolated by the smooth functions used in (11)–(13). When viscosity and surface-tension are ignored, the dynamic boundary condition of zero pressure ($p = 0$) at the free surface is also satisfied adequately by applying the irregular star method [29] to (9). The distance between the surface and the nearest fluid grid can be obtained via the density function.

The velocities, pressure and density function in a grid filled with fluid are imposed at the inflow boundary on the basis of the second-order cnoidal wave theory. We adopted a non-slip condition at the bottom boundary. As a first approximation, air bubble entrainment was ignored in this simulation, which is appropriate for the dominant fluid motion throughout the surf zone. Numerical and wave conditions corresponding to a laboratory scale are shown in Table I.

3. RESULTS

3.1. Validation procedures

To examine our numerical approach, analytical and experimental comparisons were made. As a numerical test of non-linear incident waves, cnoidal waves were generated at the inflow boundary in the numerical wave flume with a flat bottom.

Figure 3 shows the time series of surface elevation, horizontal and vertical velocity obtained numerically, experimentally and analytical results from second-order cnoidal wave theory, at

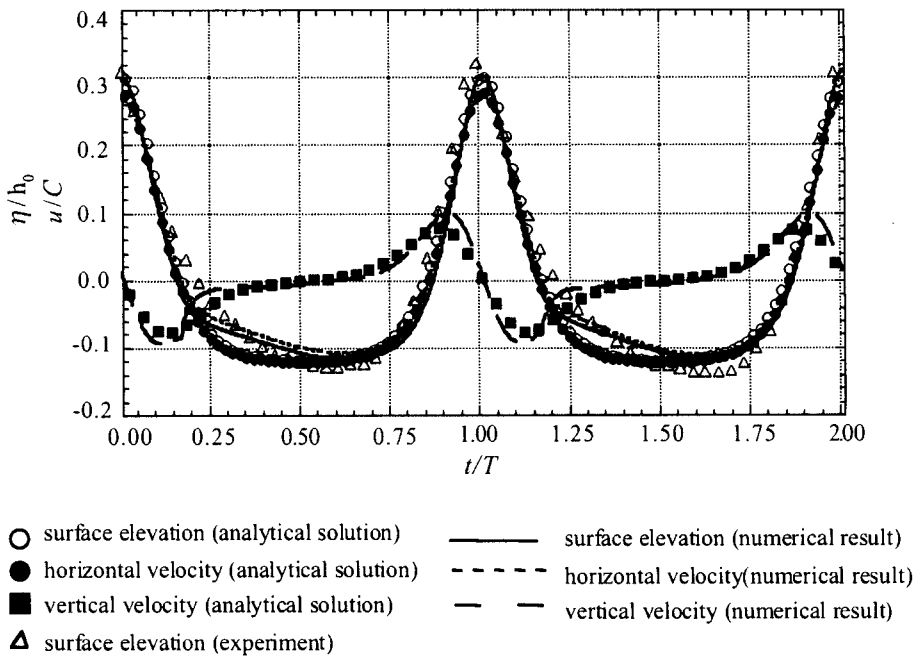

Figure 3. Time series of the surface elevation, horizontal and vertical velocity at the trough level in the test case.

the trough level. The relevant wave conditions are given in Table I. It can be seen that there is close agreement, and the non-linear incident waves are accurately generated in the numerical wave flume.

3.2. *Instantaneous velocity field*

The numerical results for the instantaneous velocity field and eddy structure after wave breaking are discussed in this section. A sequence of velocity vectors for case 3 (c.f. this case and the others specified in Table I) are plotted in Figure 4, where (a)–(g) denote successive phases at time intervals of 1/16th of the wave period after the wave breaking phase t_b—with (b), (d) and (g) representing the first, second and third plunging phase. The overturning jet in (a) can be seen to rebound at the plunging point in phase (b) and then (c), before splashing and projecting forward to hit the water ahead at the second plunging point in (d) and then (e). In (f) and (g), large-scale eddies are produced at each plunging point as the tip of jet proceeds in the splash-up cycle.

Peregrine [30] classified the splash-up and the sources of water in plunging jets visually, into the following three categories: (1) the overturning jet rebounds on previously undisturbed water, and the water in the subsequent jet comes from the overturning jet; (2) the overturning jet penetrates the surface, the previously undisturbed water is pushed up, and this water then jumps up in a jet; and (3) the jet originates from the both sources of water. In Figure 4, at first the overturning jet rebounds when the tip of jet plunges as seen in (b) and (c); and then

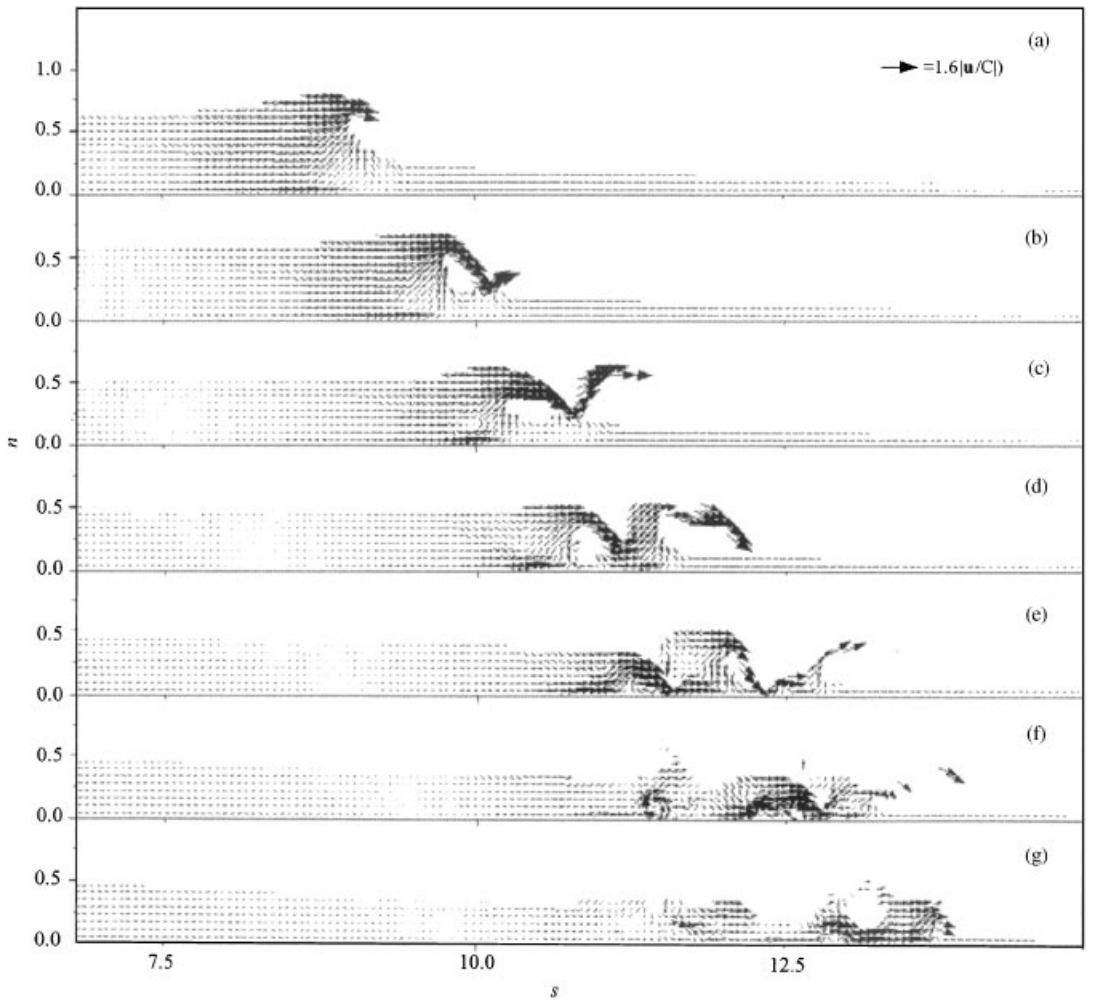

Figure 4. The velocity vector in case 3 (phase intervals; $16/T$).

in (d) and (e), the water in front of the plunging point is pushed up and the bulk of the water is lifted, due to the impulsive increase of momentum of the overturned water penetrating the surface. The splash-up type changes during one splash-up process, depending on the phase, and the jet motion evolves in the category order (1), (3) and then (2).

Figure 5 shows a photograph of the surface profile at the second plunging point, which corresponds to phase (d) in Figure 4, during experiment under the same breaking conditions ($H_b = 17.6\,\text{cm}, h_b = 14.8\,\text{cm}$). The similarity of these surface profiles further demonstrates that the jet motion during the splash-up cycle in a large-scale plunging breaker is realistically simulated. The similarities between Figures 4(d) and 5 give us further confidence in the validity of our simulation for wave breaking.

The contour of vorticity at each phase in Figure 4 is shown in Figure 6, where the solid and broken contour lines represent positive and negative vorticities, respectively. The wave

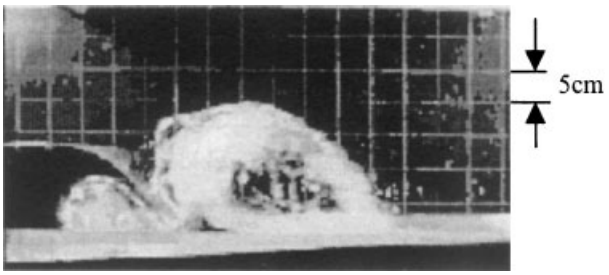

Figure 5. Photograph of the surface profile at the second plunging point during experiment (see the plunging phase (d) in Figure 6).

boundary layer is highly developed over the wide area behind the air tube in (b) and (c), and pulled up by the high shear due to the rotating fluid motion with high velocity gradient around the air tube. Then, the vorticity is separated from the boundary layer in (d), and produces the separated eddy with negative vorticity. The evolution of vorticity around the air tube in (c) and (d) causes the subsequent large-scale eddy with high shear as seen in the phase (e)–(g). The large-scale eddies first generated at each plunging point have positive (clockwise) vorticity, whereas the secondary eddies induced around the large-scale eddies have negative vorticity, due to the high shear around them. In the case shown the breaking water depth is small, and the vorticity is intensified along the bottom because it restricts the eddy advection.

Figure 7(a) shows the vorticity contour in the transition region in case 1. There are two large eddies with positive vorticity caused by the jet, and a secondary eddy in between caused by the high shear around the first large-scale eddy, as mentioned before. The generation of this secondary eddy suggests the length scale downshifts from the first large-scale eddy to the relatively small secondary eddy. The water surface near the secondary eddy is now rolled up anticlockwise, in the same direction of vorticity, which shows that the eddy structure makes a large contribution to the surface fluctuation.

The time derivative of the kinetic energy is

$$\frac{\partial E}{\partial t} = \frac{\partial}{\partial t}\left(\frac{1}{2}|\mathbf{u}|^2\right) = u\frac{\partial u}{\partial t} + v\frac{\partial v}{\partial t} \tag{15}$$

which when combined with the Navier–Stokes equation yields

$$\frac{\partial E}{\partial t} = -\nabla\left\{\mathbf{u}\left(\frac{|\mathbf{u}|^2}{2} + \frac{p}{\rho}\right) - \mathbf{u}\cdot\boldsymbol{\sigma}\right\} \underline{-\frac{1}{\mathrm{Re}}\left\{2\left(\frac{\partial u}{\partial x}\right)^2 + 2\left(\frac{\partial v}{\partial y}\right)^2 + \left(\frac{\partial u}{\partial y} + \frac{\partial v}{\partial x}\right)^2\right\}} \tag{16}$$

where $\boldsymbol{\sigma}$ denotes the stress tensor and the negative underlined terms represent energy dissipation. Figure 7(b) shows the energy dissipation contour in this case, where it can be seen that high energy dissipation occurs in the area between the first and second large-scale eddies, and between the second eddy and the bore front. The reason is that there is high shear acting in this area, because these large-scale eddies all have vorticity in the same direction. Thus the wave energy after wave breaking is dissipated not only by the direct contribution of turbulence produced at the front, but also by the interaction between the large-scale eddies.

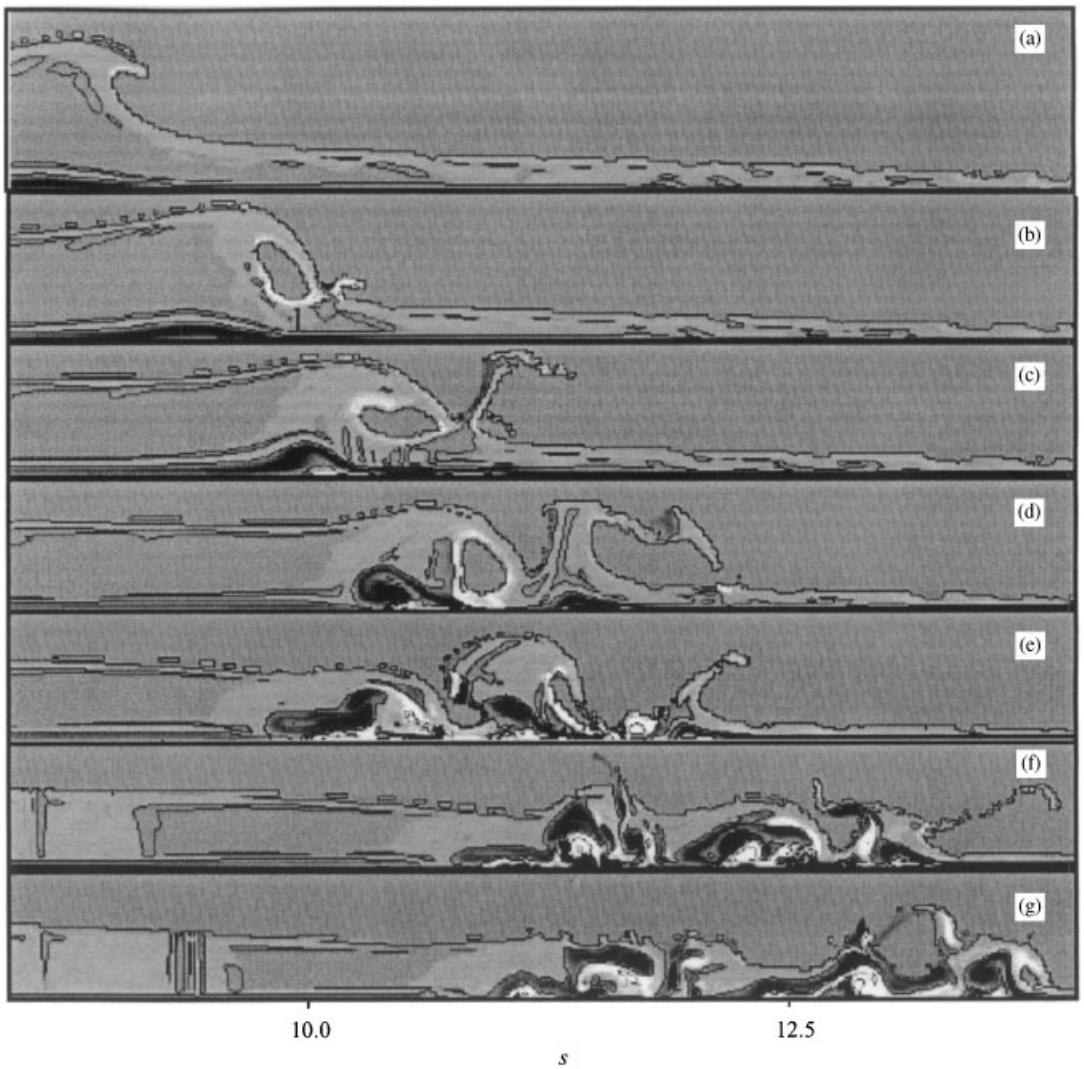

Figure 6. Contours of the vorticity in case 3 (solid contour line; positive vorticity, broken contour line; negative vorticity).

3.3. *Frequency changes*

Although the spectrum for the water surface elevation before wave breaking shows sharp energy peaks due to the non-linearity, at frequencies more than several times the basic frequency of the incident wave in shallow water [10, 31], after wave breaking these peaks become lower and smoother out as the higher frequency band contains more energy. However, the energy frequency transition as the water wave turns into the turbulent bore has been an open question. Thus in modelling the energy dissipation during wave breaking, we investigate not only

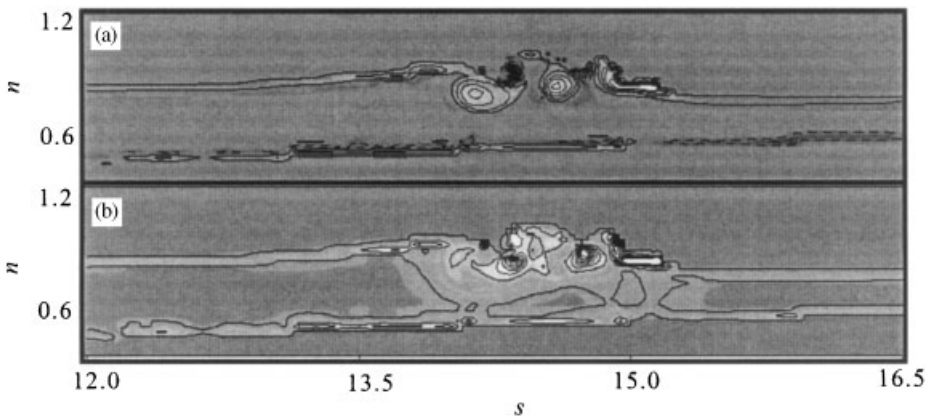

Figure 7. Contours of the vorticity (above, solid contour line; positive vorticity, broken contour line; negative vorticity) and energy dissipation (below) in the transition region in case 1.

how the wave energy is dissipated at plunging, but also how the kinetic energy spectrum associated with the waves changes in both the transition region and the bore region.

In this section, these changes are investigated for each breaker type, using frequency spectral analysis.

We consider the simulated velocity field after the sixth wave break, when the wave motion becomes sufficiently periodic and the breaking point is fixed.

Figure 8(a) shows the calculated spatial transition of typical kinetic energy ($k = \mathbf{u} \cdot \mathbf{u}/2$) spectra at the trough level near the relative depths $h/h_0 = 0.49$, 0.45 and 0.26 for case 2 (spilling breaker). The abscissa is the relative frequency for the basic frequency of the incident wave (σ_0), and the ordinate is the non-dimensional kinetic energy. It is possible to just qualitatively examine energy spectra on the basis of the present results by comparing to the spectra in experiment although the energy spectra after wave breaking immediately change in space along the wave direction. According to an experimental study [8], the velocity spectra exhibit an inertial subrange with $-3/5$ slope at high frequencies, and most of spectra in the frequency range where $\sigma/\sigma_0 > 15$ are supported by their experimental results. Some prominent energy peaks in the frequency range near $10\sigma/\sigma_0$ intermittently arise during the wave breaking process, despite the surface elevation smoothly decreasing as the front propagates, in the case of the spilling breaker (e.g. see Figure 21). These peaks all tend to shift to higher frequencies as the depth h/h_0 decreases (c.f. (a.1) and (a.3)), corresponding to a lowering of the kinetic energy. The energy spectrum at $h/h_0 = 0.45$ in (a.2) does not show the uniform slope in the frequency range $\sigma/\sigma_0 > 15$ seen in (a.1) and (a.3) however, because of the presence of the small peaks in this range. The small peak near the frequency of $10\sigma/\sigma_0$ decomposes into several smaller peaks as h/h_0 decreases, as seen in (a.3). It is also evident that the energy peaks present in the middle range (from 8 to 15 σ/σ_0) quantitatively contribute to energy transfer in the inertial subrange.

Figure 8(b) shows the trough level energy enstrophy ($= \omega \cdot \omega/2, \boldsymbol{\omega}$; vorticity) spectra, which represent an intensity of vorticity at each frequency. The frequency range near $10\sigma/\sigma_0$ also contains prominent peaks, which shows that the relatively large-scale eddies with high vorticity arise even in a spilling breaker.

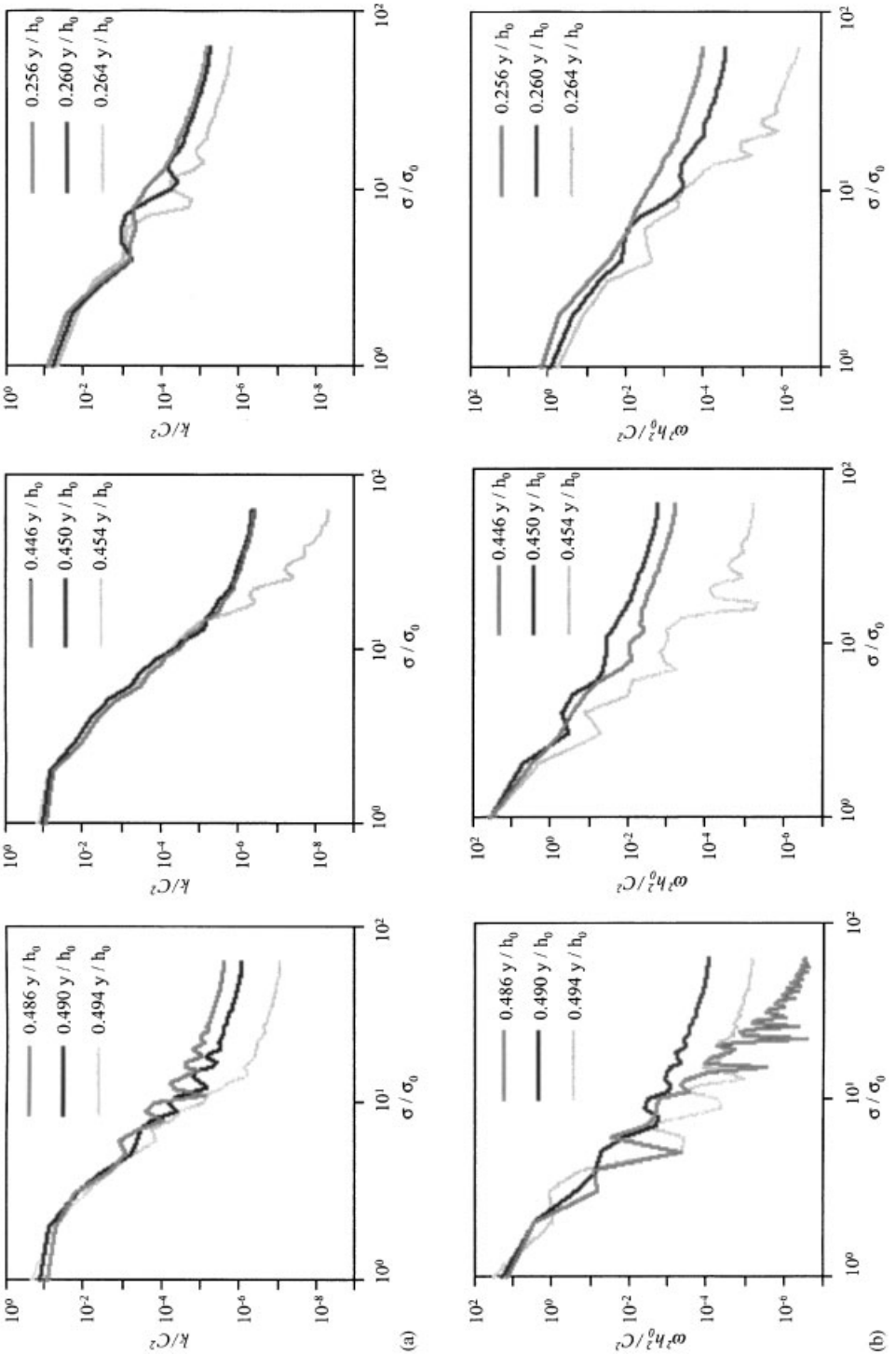

Figure 8. Typical energy spectra at the trough level in case 2; (a) kinetic energy (above), (b) enstrophy (below).

The energy spectra in the plunging breaker rapidly transform in space, especially near the plunging points. Figure 9(a) shows the typical spectra of kinetic energy at the trough level near $h/h_0 = 0.5$ (the second plunging point), near $h/h_0 = 0.48$ (just behind the second plunging point), and near $h/h_0 = 0.39$ (the fourth plunging point) in case 1 (a plunging breaker). In (a.1), prominent energy peaks arise at the harmonic frequencies $\sigma/\sigma_0 = 24$, 36, and 48. These peaks gradually decay and transfer into a higher range as the depth h/h_0 decreases. This can be seen in (a.2), where most harmonic peaks in (a.1) are significantly lower and smoother, although a broad higher peak still remains in the middle range near $10\sigma/\sigma_0$. At the fourth plunging point shown in (a.3), the first peak arising near $\sigma/\sigma_0 = 6$ for $h/h_0 = 0.386$ gradually transfers to a higher range where the energy rapidly grows, as the depth h/h_0 decreases.

The enstrophy spectra for (a) are shown in Figure 9(b). In (b.1), the spectra show many prominent peaks in the frequency range where $\sigma/\sigma_0 > 8$, and the eddy structure with high vorticity at certain frequencies is formed at the plunging point. The harmonic peaks in enstrophy also appear at the same frequencies where there are peaks in the kinematic energy spectrum—c.f. Figure 9(a.1). This suggests there is a high correlation between time scales of the vorticity fluctuation and the velocity fluctuation in the high frequency range. In (b.1) and (b.2), the large-scale eddy caused by the second plunging retains the same predominant frequencies in the middle range where $\sigma/\sigma_0 > 8$ and $\sigma/\sigma_0 < 12$. Thus we infer that the prominent vorticity fluctuation in the large-scale eddy has time scale of about 1/10th of incident wave period, and that the large-scale eddy is decomposed into smaller scale eddies with time scales (as seen in the harmonic peaks in (b.1)) associated with its time scale during the evolution of vorticity. This can be explained through the generation mechanism of the secondary eddy previously discussed in Section 3.2. The enstrophy transition seen in (b.1) and (b.2) suggests that the high enstrophy peak originates from the large-scale eddy due to the second splash, since a smaller scale eddy dissipates more rapidly. In (b.3), the very high enstrophy in the middle range transfers to high frequencies, as the spectrum evolves rapidly in space.

The inertial subrange of frequencies with an uniform slope seen in Figure 8 may exist at the higher range for the plunging breaker. The kinetic energy spectrum in a plunging breaker is evidently different from that in a spilling breaker, because of the rather higher kinetic energy in the frequency range near $10\sigma/\sigma_0$ due to the large-scale eddy.

3.4. Reynolds stress

It is possible to define the turbulence via Reynolds decomposed quantities and their correlations from our simulation, in order to understand the turbulent contribution to the mean velocity field. The production, transport and dissipation processes of Reynolds stress are discussed in this section.

A turbulence component f' is defined as a deviation from a phase-averaged quantity $\bar{f}$ of an incident wave (i.e. $f = \bar{f} + f'$). The numerical quantities at time intervals Δt were averaged over just ten periods, due to the huge data file and calculation time involved, so we should give some consideration of the statistical meaning of the phase-averaged quantities. Figure 10 shows both the maximum and the average of the relative deviation ($\varepsilon = |k_n - k_{n-1}|/k_n$) taken over all the numerical grid, where k_n denotes the kinetic energy averaged over n periods. Since both deviations are seen to converge close to 0 for $n > 6$, we find that the velocity field achieves quasi-steady state in $n > 6$ and its phase-averaged quantity does have statistical meaning.

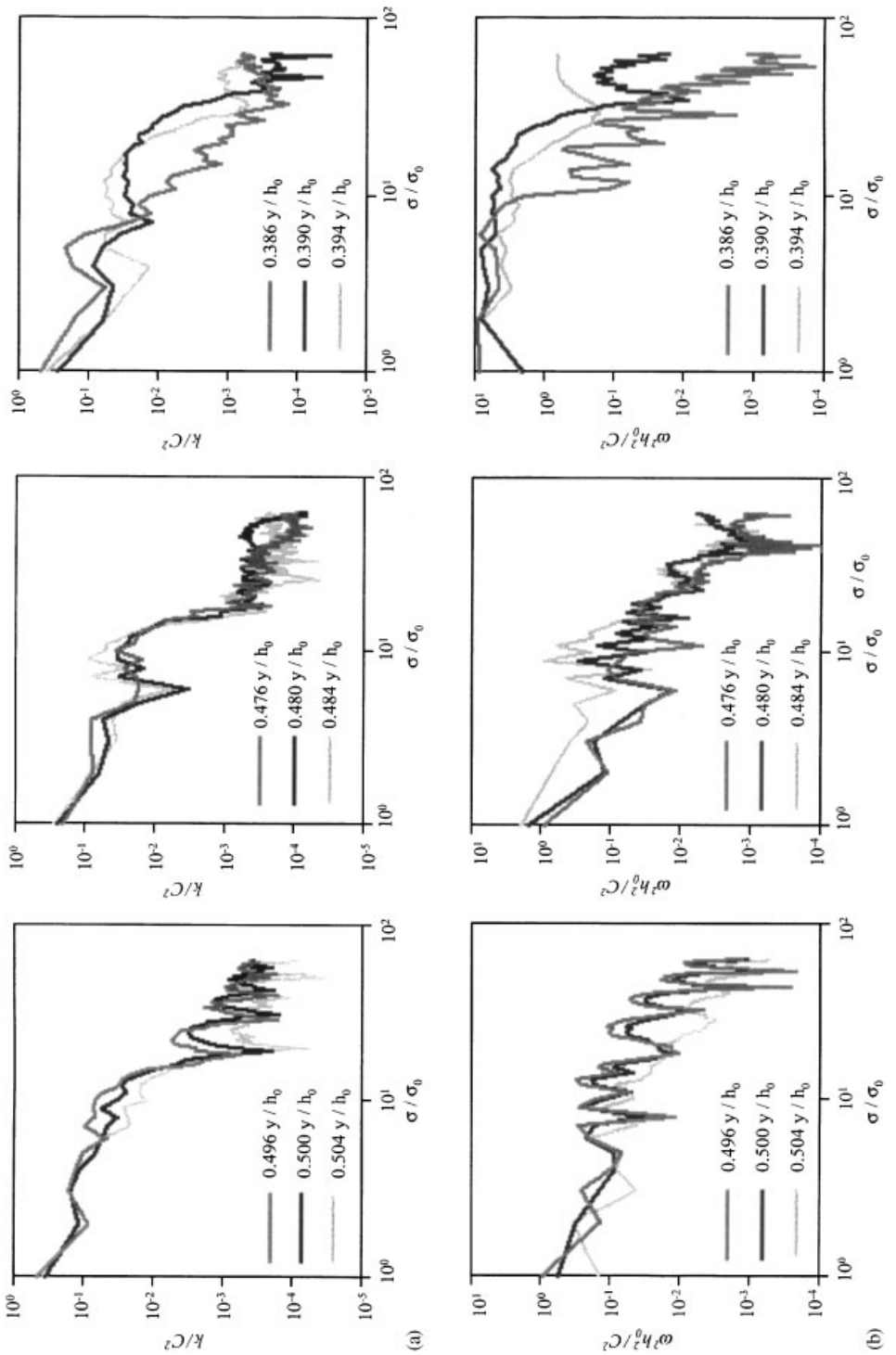

Figure 9. Typical energy spectra at the trough level in case 1; (a) kinetic energy (above), (b) enstrophy (below).

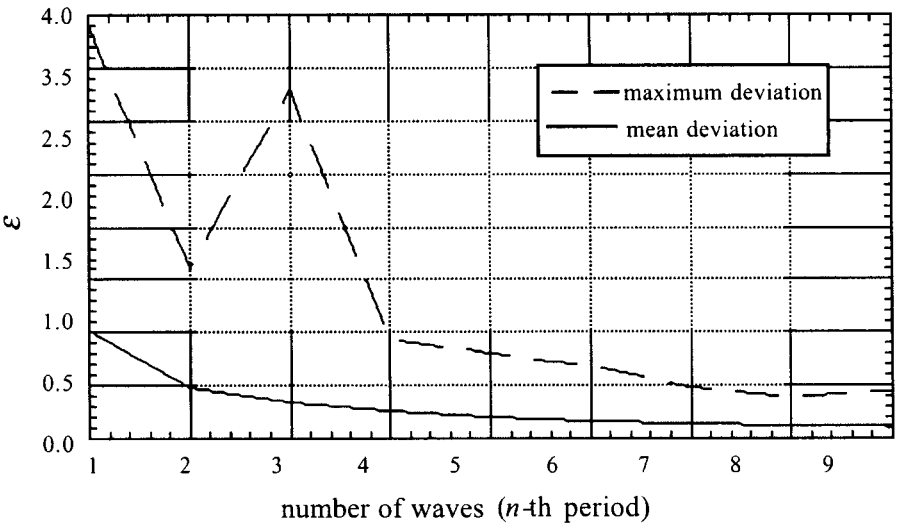

Figure 10. Relative deviations of the phase averaged kinematic energy over n periods.

Figure 11 shows the contours of each component $\overline{u'^2}$, $\overline{v'^2}$, $\overline{u'v'}$ of the Reynolds stress tensor, near the bore front in case 1 (plunging breaker). The time interval of each phase (a)–(c) is $T/4$, and the front at phase (a) is located at the third plunging point. The high intensity of the horizontal turbulent energy $\overline{u'^2}$ at the front can be seen in (a), whereas in (b) it appears that the $\overline{u'^3}$ component is diffused into the wide area behind the front, mainly above the trough level. In (c), it appears that the production of $\overline{u'^2}$ is restrained, and the turbulent energy of this component is rapidly dissipated as the bore front propagates. Since the diffused turbulence cannot advect with the front it is left behind, due to the difference in the phase-averaged fluid velocity between the front face of the bore and behind it. On the other hand, it can be seen that the vertical turbulent energy component $\overline{v'^2}$ is mainly produced below the bore front at each phase, and the component $\overline{v'^2}$ is much smaller than $\overline{u'^2}$. The large difference in intensity between the components $\overline{u'^2}$ and $\overline{v'^2}$ show that the turbulent energy retained in the front is mainly the horizontal component $\overline{u'^2}$, so the turbulence is highly anisotropic. The distribution of the deviation component $\overline{u'v'}$ is transformed in a complicated way, with the front face of the bore having positive values of $\overline{u'v'}$, and negative and positive values of $\overline{u'v'}$ arising by turn behind it. In a plunging breaker, the source of these Reynolds stress components is in the bore front, and they are not isotropically diffused from the front but left behind as locally intensified Reynolds stress because they are intermittently produced.

The horizontal and vertical mixing length scales

$$l_x^2 = \overline{u'^2} \Big/ \left(\frac{\partial U}{\partial y} + \frac{\partial V}{\partial x}\right)^2 \quad \text{and} \quad l_y^2 = \overline{v'^2} \Big/ \left(\frac{\partial U}{\partial y} + \frac{\partial V}{\partial x}\right)^2 \tag{17}$$

can also be compared.

The probability distribution of the horizontal mixing length (l_x) and the vertical (l_y) is shown in Figure 12, at the each phase in Figure 11, where values greater than 99% may be located at or behind the bore front. The horizontal length is seen to be 10 times larger

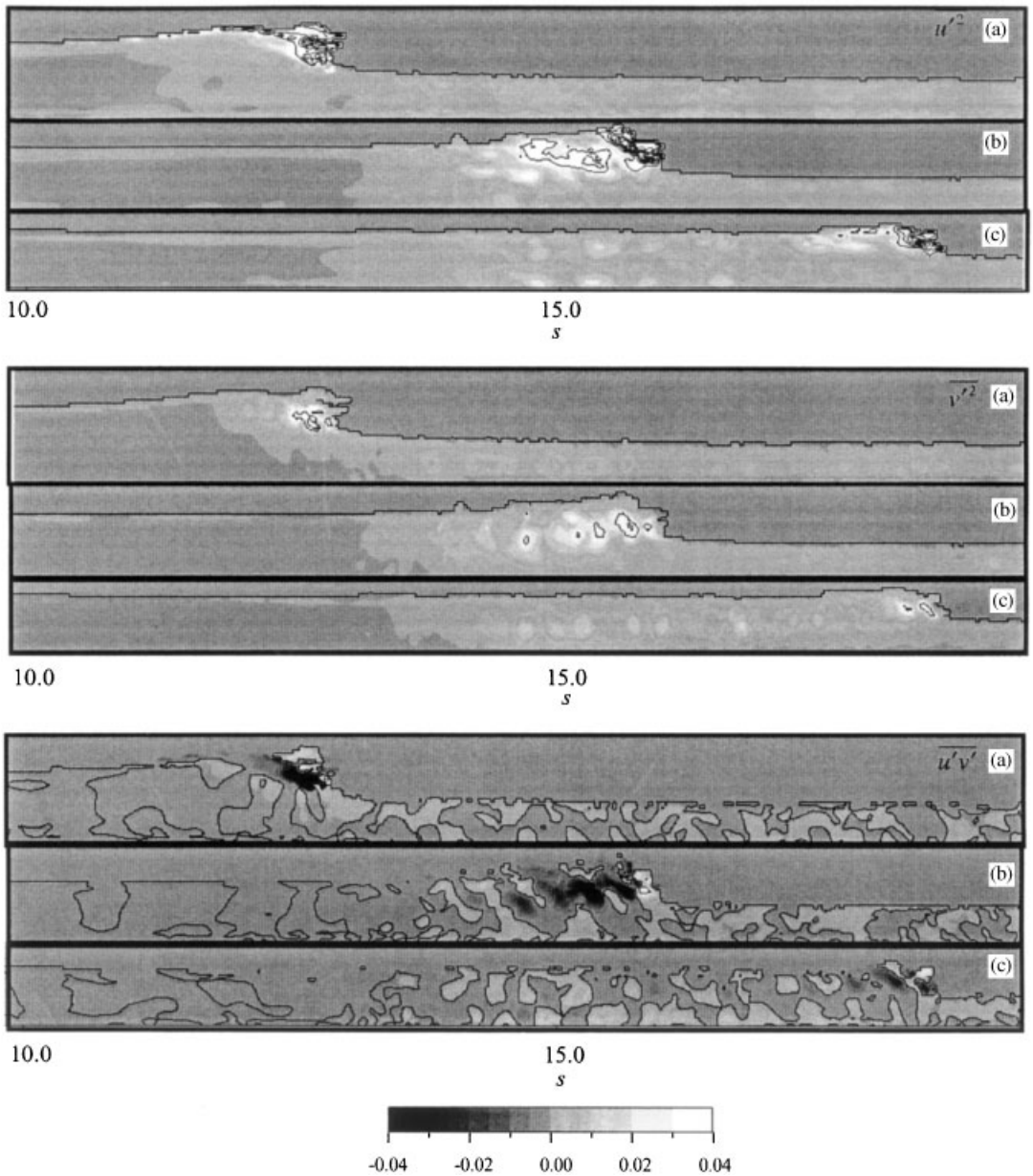

Figure 11. Contours of the Reynolds stress components; in case 1 (phase intervals; $4/T$).

greater than the vertical everywhere, again indicating that the turbulent mixing is associated with strong horizontal directivity throughout the surf zone. The maximum horizontal lengths (l_x/h_0) at each phase were 0.5285, 0.4573, 0.4173 and the maximum vertical lengths (l_y/h_0) were 0.05219, 0.08928, 0.12009, respectively. We note however that the horizontal length

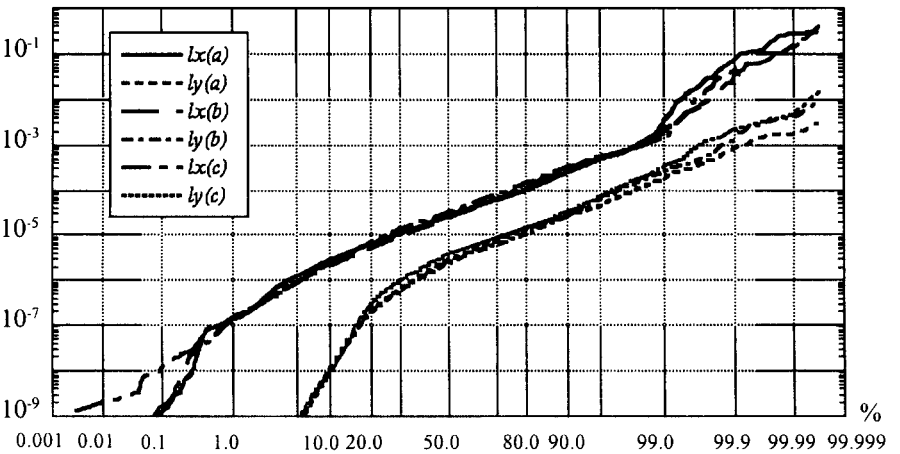

Figure 12. Probability distributions of the horizontal and vertical mixing lengths over all computational grids at the phase (a)–(c) (See Figure 13) in case 1.

gradually decreases and the vertical length increases as the bore front propagates, corresponding to turbulent energy with horizontal directivity being transferred into the vertical, during the evolution of wave breaking.

Figure 13 shows the contours of the Reynolds stress components after wave breaking in case 2 (spilling breaker), with (a)–(c) denoting each phase at time intervals of $T/4$. Each component initially produced at the wave crest in (a) markedly evolves only near the free surface behind the front, and diffuses in a narrow area near the surface as the wave breaking evolves. The horizontal turbulent energy component $\overline{u'^2}$ is however much greater than the vertical component as before; and locally intensified positive and negative values of $\overline{u'v'}$ the component occur in turn as in case 1 (plunging breaker), although their length scale is much smaller.

Many wave breaking models for a depth-averaged wave equation have been developed, by experimentally determining a suitable energy dissipation rate for incident wave energy, and assuming generated turbulence is homogeneous under steady state (see e.g. [32]). This approach is mainly applicable to a spilling breaker, where there is a close balance in turbulence production and dissipation—and for example [7] proposed a bore model based upon homogeneous turbulence. In coastal engineering for example, simple eddy viscosity models such as the linear k–ε model have been used to estimate the contribution of turbulence due to wave breaking (e.g. [33]). The simple type of the eddy viscosity model is given as

$$\begin{bmatrix} \overline{u'^2} & \overline{u'v'} \\ \overline{u'v'} & \overline{v'^2} \end{bmatrix} = \nu_T \begin{bmatrix} 2\dfrac{\overline{\partial u}}{\partial x} & \dfrac{\overline{\partial u}}{\partial y} + \dfrac{\overline{\partial v}}{\partial x} \\ \dfrac{\overline{\partial u}}{\partial y} + \dfrac{\overline{\partial v}}{\partial x} & 2\dfrac{\overline{\partial v}}{\partial y} \end{bmatrix} \tag{18}$$

where ν_T is the eddy viscosity. The above relation indicates that each component of Reynolds stress is evaluated by each phase-averaged strain tensor component isotropically multiplied by the unique ν_T for all components. In Figures 11 and 13 it is evident that the length scale of the Reynolds stress produced at the toe of the bore front can be related to the

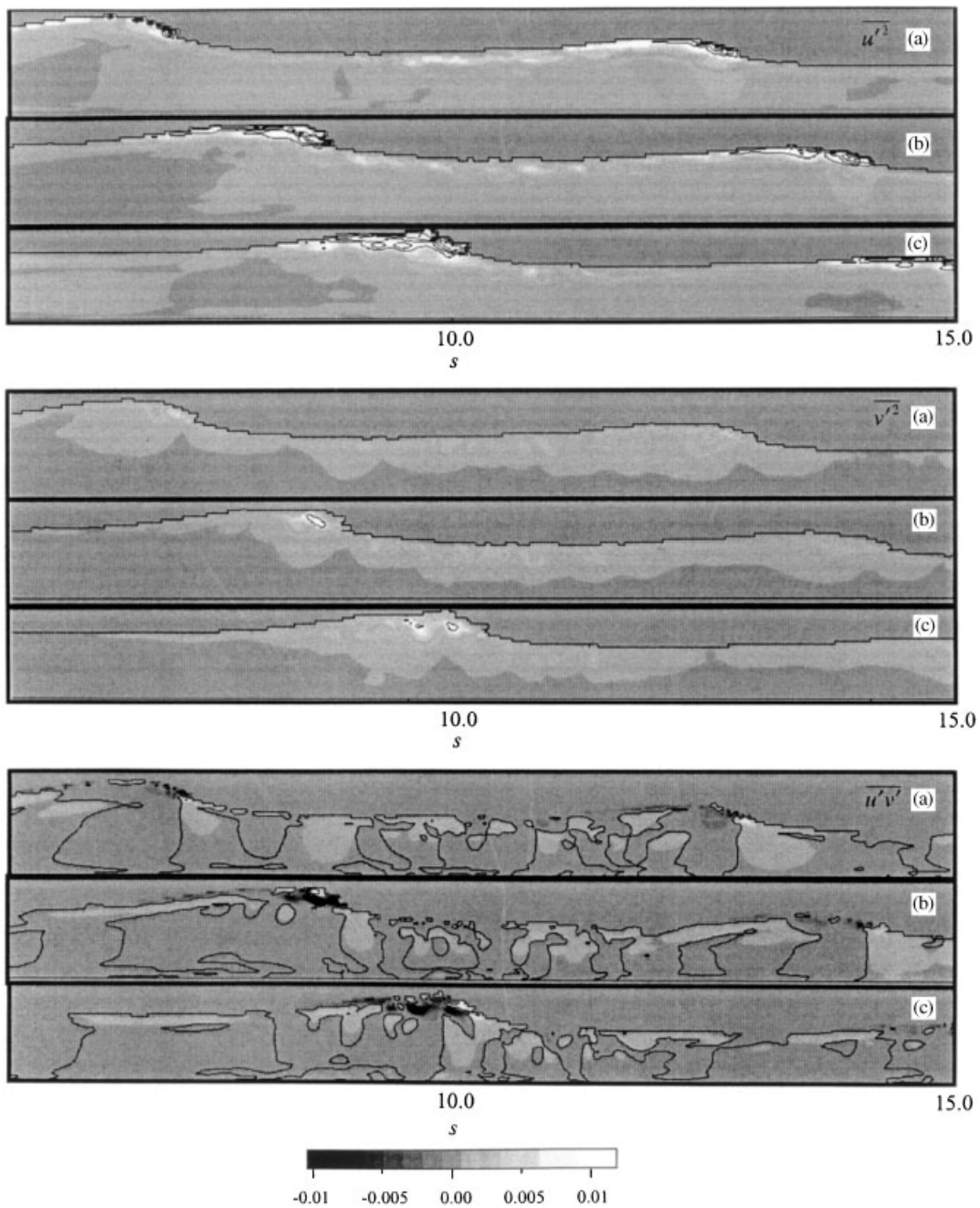

Figure 13. Contours of the Reynolds stress components in case 2 (phase intervals; $4/T$).

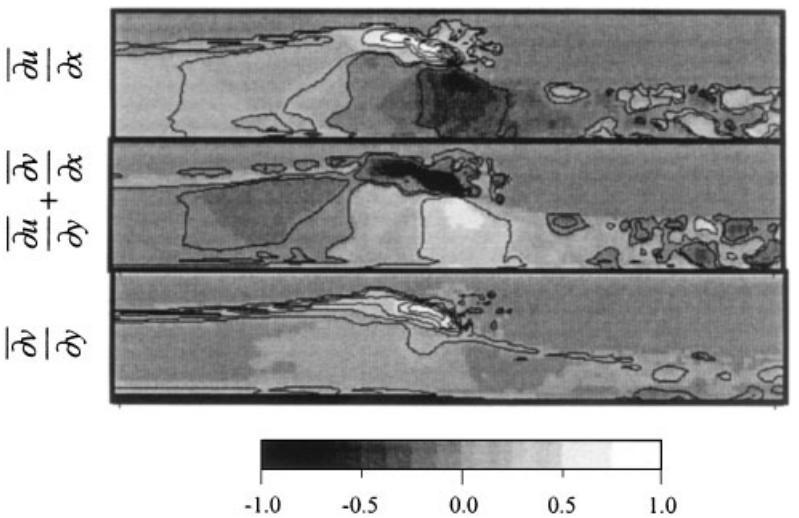

Figure 14. Contours of the strain tensor components at the phase (a) (See Figure 13) in case 1.

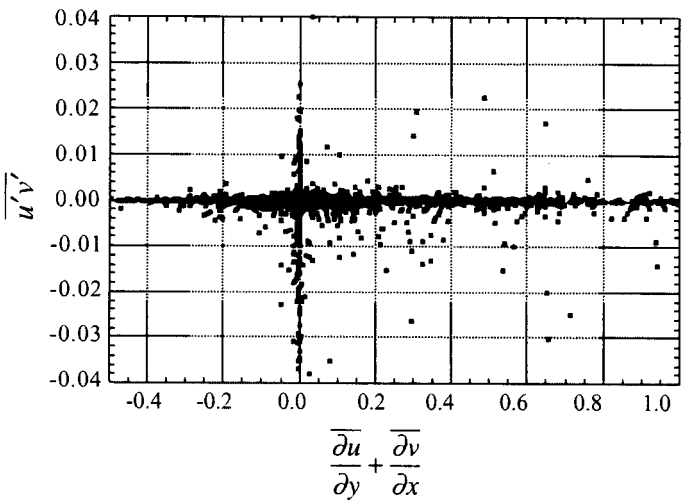

Figure 15. The Reynolds stress the strain $\overline{\partial u}/\partial y + \overline{\partial v}/\partial x$ at the phase (a) (See Figure 13).

vertical length of the front face. Figure 14 shows the contours of the phase-averaged strain tensor components; $\overline{\partial u}/\partial x, \overline{\partial u}/\partial y + \overline{\partial v}/\partial x, \overline{\partial v}/\partial y$ at the same time as in Figure 11(a). The symmetric components $\overline{\partial u}/\partial x$ and $\overline{\partial v}/\partial y$ have similar distribution, with plus and minus values, respectively, as a demanded by the continuity equation. The deviation term is smooth, with correspondingly high strain at the bore front and near the wave boundary layer, but it can be shown that any phase-averaged strain component does not correlate even qualitatively with the corresponding Reynolds stress component as in Figure 11. For example, Figure 15 shows the relation between $\overline{u'v'}$ and $\overline{\partial u}/\partial y + \overline{\partial v}/\partial x$ for all grid points, and there is no prominent

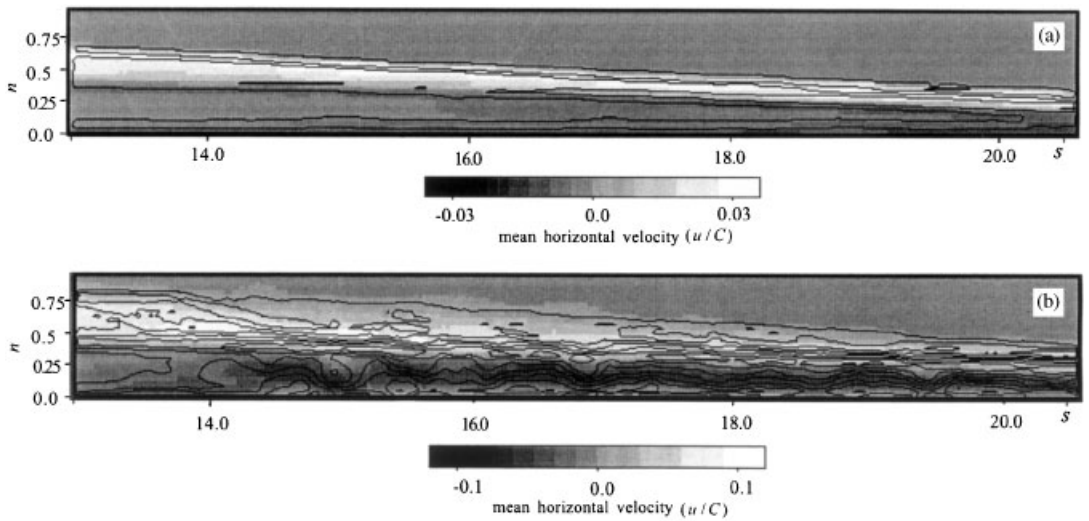

Figure 16. Streamlines for the mean velocity in case 2 (above; spilling breaker) and case 1 (below: plunging breaker).

correlation whatsoever. This demonstrates that the strain components may not be isotropically multiplied by a single eddy viscosity coefficient, as in (18), to express the Reynolds stress tensor. Thus although a simple isotropic linear k–ε model may apply in the inertial range, it cannot apply to the anisotropic and unsteady flow field in the surf zone of a breaking wave where there is horizontally dominated turbulence, especially near the bore and large-scale eddies.

3.5. Mean velocity field

On a sandy beach, a mean flow velocity such in a nearshore current or undertow can produce significant sand drift, or transport of suspended sand above the sea bottom. Mean flow velocities have been investigated experimentally by many researchers (e.g. [8]), to estimate the mean fluid force acting on sediments. Watanabe and Mori [34] reported that the turbulent energy after wave breaking is intensified by the presence of undertow, especially in a plunging breaker. As a first step in modelling relevant velocity profiles, the mean velocity field accompanying each breaker type is now examined.

The fluid velocity was averaged over ten periods, for both case 2 (spilling breaker) and case 1 (plunging breaker), and the streamline for the mean velocity is shown in Figures 16(a) and (b), respectively. The background colour denotes mean horizontal velocity. In Figure 16(a), the horizontal component is positive (shoreward) above the trough level and negative underneath, much greater than the vertical component, and smoothly varying throughout the surf zone. The undertow associated with offshore-ward velocity is intensified in very shallow water, to return the momentum transported in by the bore front back offshore. On the other hand, in Figure 16(b) the mean velocity vertically fluctuates on the scale of the water depth underneath the trough level in the transition region. Although the vertical velocity component has commonly been regarded as very much smaller than the horizontal, and ignored in estimating

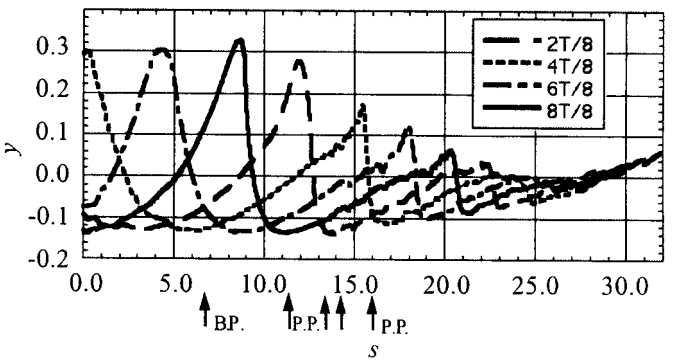

Figure 17. The surface elevation in case 1.

the effect of the mean velocity flow, there is now vertically fluctuating undertow caused by the large-scale eddies.

Decomposing instantaneous quantities into time-averaged, phase-averaged and turbulent quantities as $u_i = U_i + \tilde{u}_i + u_i'$, $p = P + \tilde{p} + p'$, we can obtain the following momentum equation for time-averaged velocity via phase and time averaging processes for the Navier–Stokes equation.

$$U_j \frac{\partial U_i}{\partial x_j} = \frac{\partial}{\partial x_j}\left(-\frac{p}{\rho}\delta_{ij} + v\frac{\partial U_i}{\partial x_j} - \overline{u_i' u_j'} - \overline{\tilde{u}_i' \tilde{u}_j'}\right) \tag{19}$$

According to Figure 11, it can be seen in a plunging breaker that the locally intensified Reynolds stress scatteredly arises in the transition region. The Reynolds stress with large spatial gradient contributes to the third term in (19), and then the mean rotational motion involving prominent mean vertical velocity is intermittently induced as shown in Figure 16. Thus the Reynolds stress in the vicinities of large-scale eddies and this spatial variation cannot be ignored in case of a plunging breaker, in estimating the effect of its undertow.

3.6. Wave number properties

After wave breaking, the fluid motion generally can be assumed periodic in time at any fixed point, but it is non-uniform in space because the evolving turbulence is irreversible. To model a breaking wave, we must evaluate the spatial change of the wave number in the velocity field as well as the frequency variation, during the evolution process of wave breaking and turbulence. It is not possible to appropriately estimate spatial changes of wave numbers of velocity fluctuation by frequency spectrum analysis because of irreversible evolutions of wave breaking. In this section, we discuss correlations and spatial length scales in the wave number energy spectra for the surface elevation, the phase-averaged kinetic energy, and the turbulent energy throughout the surf zone.

Figure 17 shows the spatial distribution of the phase-averaged surface elevation at four successive $T/4$ intervals for case 1 (plunging breaker). Since the surface elevation is defined as the density function integrated over depth, the surface profile with an overturning jet is not considered here, but this figure shows that the surface profiles are transformed with the steep front decreasing the wave height. The phase-averaged kinetic energy integrated over the

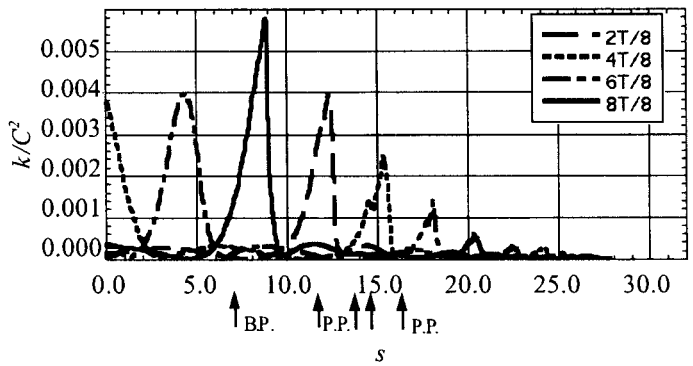

Figure 18. The phase-averaged kinetic energy integrated over depth in case 1.

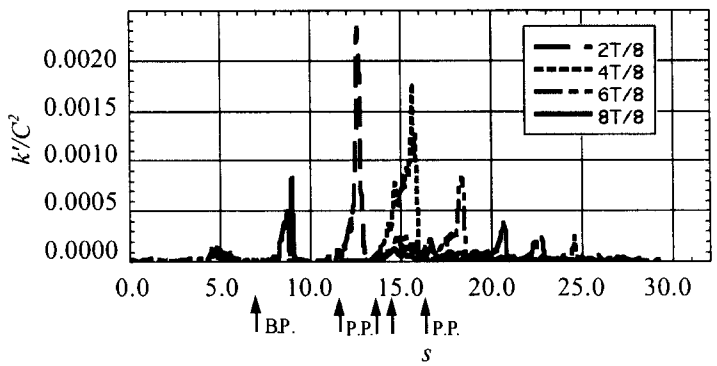

Figure 19. The turbulent energy integrated over depth in case 1.

depth is shown in Figure 18. The kinetic energy integrated over the depth must correlate with the square of the surface elevation, if the kinetic and potential energy were in approximate equilibrium. However, it is evident that their peaks change at a different rate in the wave direction after wave breaking so there is clearly no such equilibrium, which indicates that the phase-averaged velocity field cannot be estimated only from the surface elevation and must also be taken into account in sufficient modelling the turbulence. Figure 19 shows the turbulent energy integrated over depth in this case, where a steep high energy peak arises at the front of the broken wave and diffuses behind the front after $4T/8$.

Figures 20–22 show the phase-averaged surface elevation, the phase-averaged kinetic energy integrated over depth and the turbulent energy integrated over depth in case 2 (spilling breaker). Each result exhibits smooth decay after wave breaking, and the production of turbulence is both weak and slow and almost in balance with the dissipation, in this case. The intermittent intensity of turbulence energy as seen in the transition region ($x/h_0 = 5$–15) in Figure 22 is possibly associated with the vorticity fluctuated with the frequency in the middle range which we discussed in Section 3.3.

To evaluate the spatial characteristics of these breaking waves, the wave number properties of the surface elevation and the kinetic energy were analysed by wavelet transform,

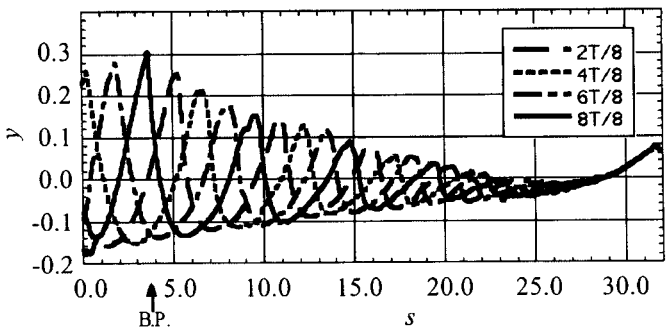

Figure 20. The surface elevation in case 2.

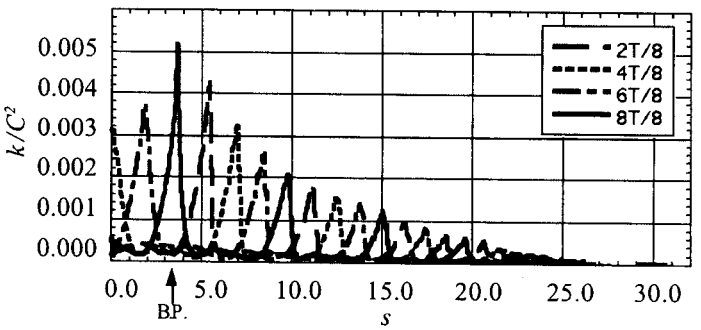

Figure 21. The phase-averaged kinetic energy integrated over depth in case 2.

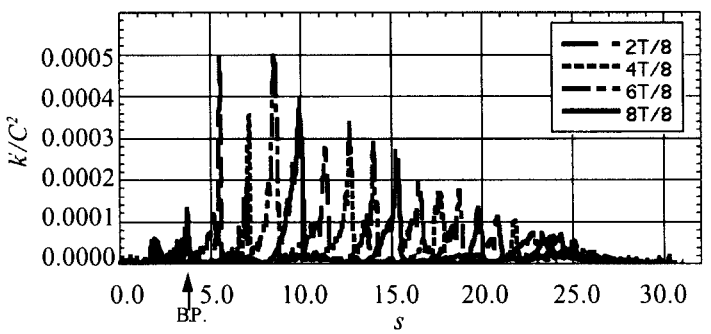

Figure 22. The turbulent energy integrated over depth in case 2.

which efficiently filters unsteady phenomena with sudden changes into suitable wave number spectra [35].

The wavelet coefficient is defined by

$$W_{\mathrm{f}}(b,a) = \int_{-\infty}^{\infty} \frac{1}{\sqrt{|a|}} f(x)\psi\left(\frac{x-b}{a}\right) \mathrm{d}x \tag{20}$$

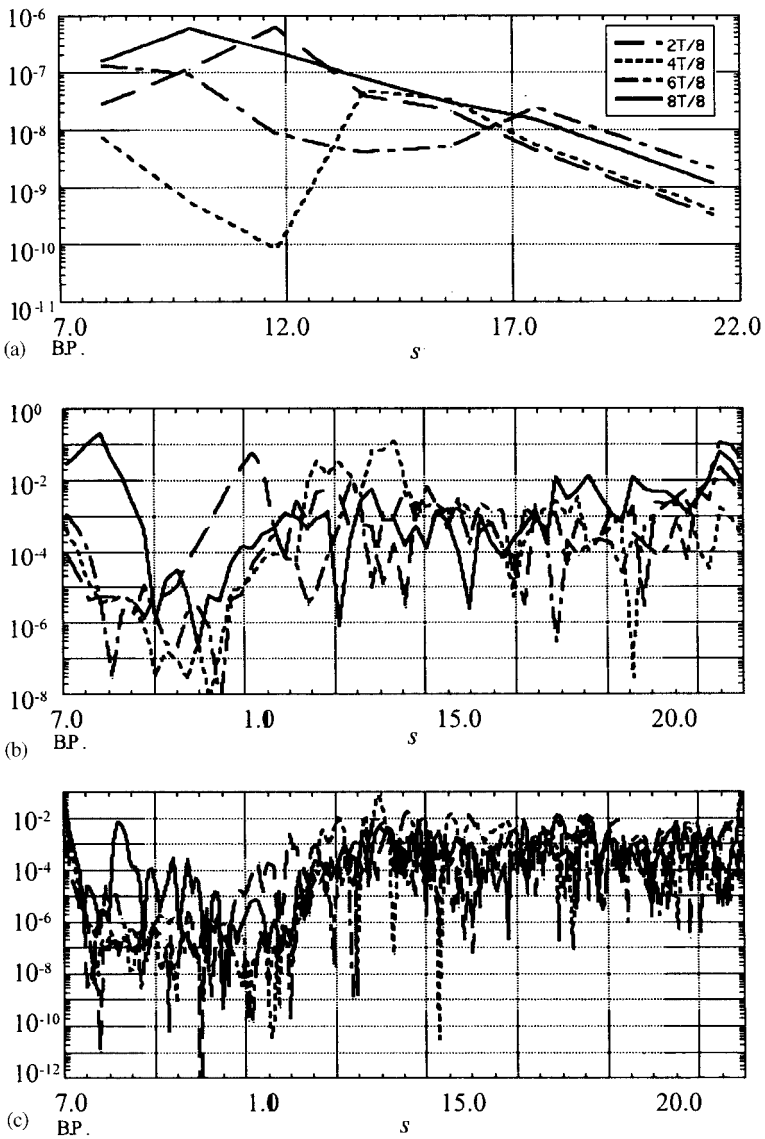

Figure 23. Wavelet spectra of the surface elevation; (a) non-dimensional wave number $k_w = 3.27$, (b) $k_w = 26.18$, and (c) $k_w = 104.67$.

where $f(x)$ is an arbitrary function in x, ψ is a mother wavelet, the scale dilation parameter a and the translation parameter b. In the present analysis, the third-order cardinal B-spline function which has a high resolution is used as the wavelet basis. With the parameteric pair $(b, 1/a)$ as $(2^{-j}i, 2^j)$ where j and i are integers, the discrete wavelet coefficient is

$$f_{ji} = 2^j \int \overline{\psi(2^j x - i)}\, f(x)\, \mathrm{d}x \tag{21}$$

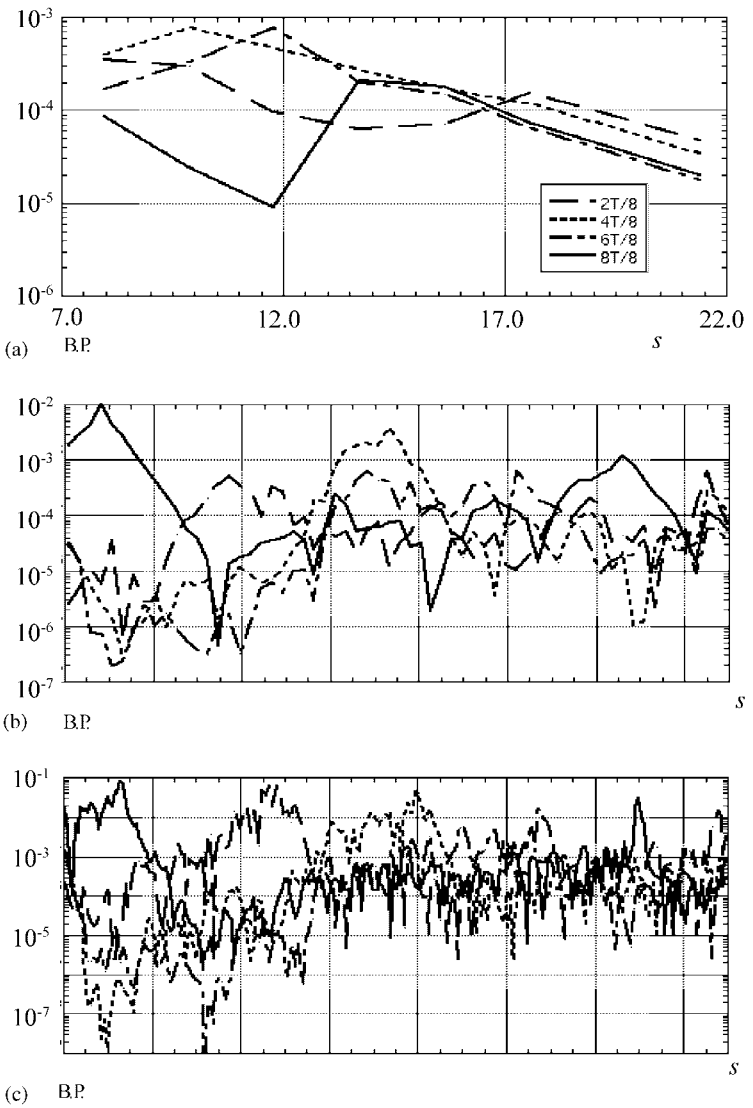

Figure 24. Wavelet spectra of the phase averaged kinematic energy integrated over depth; (a) $k_w = 3.27$, (b) $k_w = 26.18$, and (c) $k_w = 104.67$.

The local wavelet energy spectrum normalized by scaling the wave number is defined by the following relation, using the wavelet coefficient W_f:

$$dE_f = |W_f(b,a)|^2 \frac{da\,db}{a^2} \tag{22}$$

At each wave number, the spatial change in the wavelet spectrum for the energy during the wave breaking process in a plunging breaker demonstrates the characteristics of the spatial energy transfer.

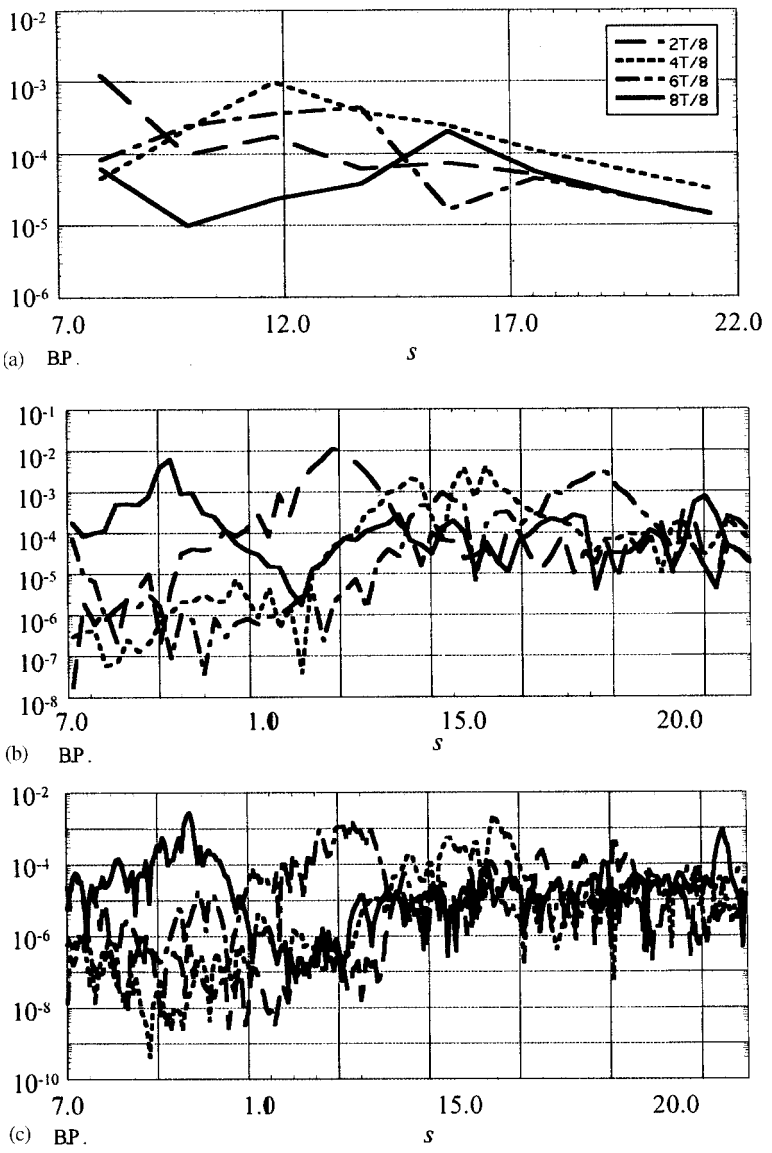

Figure 25. Wavelet spectra of the turbulent energy integrated over depth; (a) $k_w = 3.27$, (b) $k_w = 26.18$, and (c) $k_w = 104.67$.

Figure 23 shows the wavelet spectra of the surface elevation at the dimensionless wave numbers (a) $k_w = 3.27$, (b) $k_w = 26.18$ and (c) $k_w = 104.67$ at each stage in Figure 17. In (a), where the length scale is about $2h_0$, the wave height in the wave number range of the incident waves gradually decreases in the wave direction (s). In (b), where the length scale is the breaking wave height, the broad peak at each stage propagates along with the wave front in the transition region ($7.0 < s < 15$), and then the peak ahead is rapidly dissipated in

the shoreward bore region side of $s = 15$. In (c), where there is a very small length scale of $0.06h_0$, the predominant peak in (b) cannot be found in the transition region ($s < 15$), and the small scale disturbances at surface level in the bore region ($s > 15$) have higher energy than the energy in the transition region. These results indicate a progressive downshift of the length scale of the surface fluctuation.

Figure 24(a), (b) and (c) show the wavelet spectra of the phase-averaged kinetic energy integrated over depth at each wave number. The low wave number component (a) presents similarities with the wave energy transfer behaviour of Figure 23(a). The wavelet energy at $k_w = 26.18$ (See Figure 24(b)) exhibits broad peaks similar to those in Figure 23(b), but with a different dissipation rate in the transition region; the peaks do not dissipate and retain relatively high energy over a wide area even in the bore region, which differs from the surface elevation spectrum. The small fluctuation with high energy in (c) is produced near the plunging point and is advected by the front, which is also characteristically different from the results at the same wave number for the surface. These results demonstrate that the length scales of the phase-averaged surface elevation and kinetic energy do not correlate at higher wave numbers throughout the surf zone. The spectra for the turbulent energy integrated over depth are shown in Figure 25, and suggest that the turbulence is intensified at and advected by the bore front, for all wave numbers. The development and diffusion of the turbulent energy at any wave number do not correlate with the previous results.

4. CONCLUSIONS

The actual jet motion during the splash-up cycle and the velocity field during wave breaking in a large-scale plunging breaker are realistically simulated by our numerical simulation, which was initially validated against both an analytical solution and preliminary experiments. The splash-up at the plunging point changes during one splash-up process, depending on the phase, and a jet evolves as follows. At first, the overturning jet rebounds at the undisturbed water surface ahead, and then a jet toe is propelled up toward a second plunging point. Next, both the original overturning water and the forward water are propelled up, following the toe of jet. Finally, the overturned water penetrates the forward surface, and then the water in front is pushed up.

At the plunging point, the wave boundary layer is highly evolved over a wide area behind the air tube, and pulled up by the upward high velocity circulating around the tube. Although large-scale eddies directly generated by the jet at each plunging point have positive (clockwise) vorticity, the secondary eddies induced around any large-scale eddies have negative vorticity, because of high shear around the large-scale eddies. The water surface near such a secondary eddy is rolled up anticlockwise, in the same sense as the vorticity in the eddy. The eddy structure makes a large contribution to surface fluctuation. High energy dissipation occurs in the area between the large-scale eddies, due to the high shear acting there because these large-scale eddies all have vorticity in the same direction.

In a spilling breaker, the kinetic energy spectra show an inertial subrange with a uniform slope at frequencies higher than $\sigma/\sigma_0 = 15$, as found experimentally [10]. Energy peaks in the middle range from 8 to 15 σ/σ_0 significantly contribute to spectrum in the inertial subrange, and these peaks are transfer to a higher range as the depth h/h_0 decreases.

In a plunging breaker, the energy rapidly transforms in space, especially near the plunging points. Prominent kinetic energy peaks arising at harmonic frequencies are induced by velocity fluctuations associated with the large-scale eddies in the neighbourhood of $\sigma/\sigma_0 = 12$, and these harmonic peaks gradually decay and transfer to a higher range as the depth h/h_0 decreases.

In the bore region, the source of Reynolds stress is the bore front, and its components do not homogeneously diffuse away from the front but remain behind as intermittently intensified local Reynolds stress. The horizontal mixing length is everywhere much greater than the vertical (one over 10 times), indicating that turbulence has strong horizontal directivity in the transition region.

The horizontal length gradually decreases and the vertical length increases as the bore front propagates, so the directivity of the turbulent energy transfers from horizontal to vertical during the evolution of wave breaking. In a spilling breaker, successive local intensities of positive and negative component of $\overline{u'v'}$ also arise behind the bore front, although their length scale is much smaller than in the plunging breaker.

The phase-averaged strain components do not correlate even qualitatively with the corresponding Reynolds stress component, so a model where the strain components are isotropically multiplied by a unique eddy viscosity (such as in (18)) is unacceptable.

The wavelet spectrum analysis was carried out in order to investigate the wave number transitions of surface elevation, kinetic energy and turbulent energy in the wave direction, and the correlations between them. Although both the surface elevation and kinetic energy wavelet spectra fluctuations with larger length scale gradually decrease as the bore propagates, both increase at smaller length scales due to scaling down from the large-scale fluctuation, especially in the bore region. In particular, the surface elevation spectrum in the wave front dissipates faster in the low wave number range compared with the kinetic energy, and their spatial energy transition at any phase in the high wave number range are not correlated. Thus the velocity field after wave breaking cannot be directly estimated only from the surface elevation, and turbulence must be introduced more appropriately into any depth-averaged equations to evaluate the velocity field of breaking waves in the surf zone.

ACKNOWLEDGEMENTS

We express our gratitude to Professor Roger J. Hosking, who read the first draft of this paper and made various helpful suggestions. We also wish to thank Professor Wataru Kioka and Professor Philip L-F Liu for giving us valuable advice.

REFERENCES

1. Iversen HW. Waves and breakers in shoaling water. *Proceedings of the 3rd Conference on Coastal Engineering* 1952; 1–12.
2. Longuet-Higgins MS, Stewart RW. Radiation stress and mass transport in gravity waves with application to 'surf-beat'. *Journal of Fluid Mechanics* 1962; **8**:565–583.
3. Longuet-Higgins MS. Longshore currents generated by obliquely incident sea waves. Parts 1 and 2. *Journal of Geophysical Research* 1970; **81**:3079–3094.
4. LeMéhaute B. On non-saturated breakers and wave run-up. *Proceedings of the 8th International Conference on Coastal Engineering* 1962; 77–92.
5. Thornton EB, Guza RT. Transformation of wave height distribution. *Journal of Geophysical Research* 1983; **88**:5925–5938.
6. Battjes JA. Surf-zone dynamics. *Annual Review of Fluid Mechanics* 1988; **20**:257–293.
7. Svendsen IA, Madsen PA. A turbulent bore on a beach. *Journal of Fluid Mechanics* 1984; **148**:73–96.

8. Okayasu A, Shibayama T, Horikawa K. Vertical variation of undertow in the surf zone. *Proceedings of the 21st International Conference on Coastal Engineering* 1988;478–491.
9. Speziale CG. On non-linear K-l and K-e models of turbulence. *Journal of Fluid Mechanics* 1987; **178**: 459–475.
10. Ting FCK, Kirby JT. Dynamics of surf-zone turbulence in a spilling breaker. *Coastal Engineering* 1996; **27**:131–160.
11. Okayasu A, Shibayama T, Mimura N. Velocity field under plunging breaker. *Proceedings of the 20th International Conference on Coastal Engineering* 1986; 660–674.
12. Stive MJF. Energy dissipation in wave breaking on gentle slope. *Coastal Engineering* 1984; **8**:99–127.
13. Sakai T, Mizutani T, Tanaka H, Tada Y. Vortex formation in plunging breaker. *Proceedings of the 20th International Conference on Coastal Engineering* 1986; 711–723.
14. Park JC, Miyata H. Numerical simulation of the non-linear free-surface flow caused by breaking waves. *FED* 1994; **181**; Free-Surface Turbulence, ASME: 155–168.
15. Lin P, Liu PL-F. A numerical study of breaking waves in the surf zone. *Journal of Fluid Mechanics* 1998; **359**:239–264.
16. Lin P, Liu PL-F. Turbulence transport, vorticity dynamics, and solute mixing under plunging breaking waves in surf zone. *Journal of Geophysical Research* 1998; **103**:15677–15694.
17. Borthwick A. Comparison between two finite-difference schemes for computing the flow around a cylinder. *International Journal for Numerical Methods in Fluids* 1986; **6**:275–290.
18. Yabe T, Aoki T. A universal solver for hyperbolic equations by Cubic-Polynomial Interpolation I. One-dimensional solver. *Computer Physics Communications* 1991; **66**:219–232.
19. Yabe T, Ishikawa T, Wang PY, Aoki T. A universal solver for hyperbolic equations by Cubic-Polynomial Interpolation I. Two- and three-dimensional solvers. *Computer Physics Communications* 1991; **66**:233–242.
20. Yabe T, Wang P. Unified numerical procedure for compressible and incompressible fluid. *Journal of the Physical Society of Japan* 1991; **60**:2105–2108.
21. Nadaoka K, Hino M, Koyano Y. Structure of the turbulent flow field under breaking waves in the surf zone. *Journal of Fluid Mechanics* 1989; **204**:359–387.
22. Meijierink JA, van der Vorst HA. Guidlines for the usage of incomplete decompositions in solving set of linear equations as they occur in practical problems. *Journal of Computer Physics* 1981; **44**:134–155.
23. Hackbusch W. Convergence of multi-grid iterations applied to difference equations. *Mathematics of Computation* 1980; **34**:425–440.
24. Hackbusch W. Multi-Grid Methods and Applications. Springer: Berlin, 1985.
25. Brooks AN, Hughes TJR. Streamline upwind/Petrov–Galerkin formulations for convection dominated flows with particular emphasis on the incompressible Navier–Srokes equations. *Computer Methods in Applied Mechanics and Engineering* 1982; **32**:199–259.
26. Scardovelli R, Zaleski S. Direct numerical simulation of free-surface and interfacial flow. *Annual Review of Fluid Mechanics* 1999; **31**:567–603.
27. Thome MF, Castelo A, Murakami J, Cuminato JA, Minghim R, Oliveira MCF, Mangiavacchi N, McKee S. Numerical simulation of axisymmetric free surface flows. *Journal of Computational Physics* 2000; **157**: 441–472.
28. Hirt CW, Nichols BD. Volume of Fluid (VOF) method for the dynamics of free boundaries. *Journal of Computational Physics* 1981; **39**:201–225.
29. Chan ROC, Street RLA. Computer study of finite amplitude water waves. *Journal of Computational Physics* 1970; **6**:68–94.
30. Peregrine DH. Breaking waves on beaches. *Annual Review of Fluid Mechanics* 1983; **15**:149–178.
31. Su MY, Bergin M, Marler P, Myrick R. Experiments on non-linear instabilities and evolution of steep gravity-wave trains. *Journal of Fluid Mechanics* 1982; **124**:45–72.
32. Church JC, Thornton EB. Effects of breaking wave induced turbulence within a longshore current model. *Coastal Engineering* 1993; **20**:1–28.
33. Johnson BD, Kobayashi N, Cox DT. Formulation and validation of vertically 2-D shallow-water wave model. *Proceedings of the 25th International Conference on Coastal Engineering* 1996:551–564.
34. Watanabe Y, Mori N. Three-dimensional characteristics of velocity field and effects of undertow in a surf zone. *Proceedings of the 7th International Offshore and Polar Engineering Conference* 1997:247–253.
35. Farge M. Wavelet transforms and their applications to turbulence. *Annual Review of Fluid Mechanics* 1992; **24**: 395–457.

